PERGAMON

International Journal of Solids and Structures 39 (2002) 6135–6157

INTERNATIONAL JOURNAL OF SOLIDS and STRUCTURES

www.elsevier.com/locate/ijsolstr

Three-dimensional modeling of intersonic shear-crack growth in asymmetrically loaded unidirectional composite plates

C. Yu [a], A. Pandolfi [b], M. Ortiz [a,*], D. Coker [a], A.J. Rosakis [a]

[a] *Graduate Aeronautical Laboratories, California Institute of Technology, Mail Stop 105-50, Pasadena, CA 91125, USA*
[b] *Dipartimento di Ingegneria Strutturale, Politecnico di Milano, 20133 Milano, Italy*

Received 20 November 2001

Abstract

An anisotropic cohesive model of fracture is applied to the numerical simulation of Coker and Rosakis experiments (2001). In these experiments, a unidirectional graphite–epoxy composites plate was impacted with a projectile, resulting in an intersonic shear-dominated crack growth. The simulations account for explicit crack nucleation—through a self-adaptive remeshing procedure—crack closure and frictional sliding. The parameters used in the cohesive model are obtained from quasi-static fracture experiments, and successfully predict the dynamic fracture behavior. In keeping with the experiments, the calculations indicate that there is a preferred intersonic speed for locally steady-state growth of dynamic shear cracks, provided that sufficient energy is supplied to the crack tip. The calculations also show that the crack tip can attain speeds in the vicinity of the longitudinal wave speed in the direction of the fibers, if impacted at higher speeds. In addition, a double-shock which emanates from a finite size contact region behind the crack tip is observed in the simulations. The predicted double-shock structure of the near-tip fields is in close agreement with the experimental observations. The calculations additionally predict the presence of a string of surface hot spots which arise following the passage of the crack tip. The observed and computed hot spot structures agree both in geometry as well as in the magnitude of the temperature elevation. The analysis thus suggests intermittent friction as the origin of the experimentally observed hot spots.

Keywords: 3D finite elements; Anisotropic cohesive element; Frictional contact; Intersonic shear crack growth; Unidirectional composites; Self-adaptive remeshing

1. Introduction

Dynamic crack growth along weak planes is a significant mode of failure in composites and other heterogeneous layered materials. In recent years, bimaterial fracture specimens, fabricated by the bonding

* Corresponding author. Tel.: +1-626-395-4530; fax: +1-626-304-0175.
E-mail address: ortiz@madrid.caltech.edu (M. Ortiz).

0020-7683/02/$ - see front matter © 2002 Elsevier Science Ltd. All rights reserved.
PII: S0020-7683(02)00466-3

of a stiff to a compliant material, have been used to demonstrate the occurrence of highly transient and dynamic crack growth along preferred crack paths in heterogeneous solids. For instance, it has been observed that dynamic interfacial cracks are shear dominated, and that their speeds rapidly approach, and exceed, the shear wave speed of the more compliant material (Lambros and Rosakis, 1995b; Liu et al., 1995; Rosakis et al., 1998; Singh et al., 1997; Singh and Shukla, 1996). Thus, these cracks reach intersonic speeds with respect to the lower wave speed constituent of the composite. In the present context, intersonic crack-tip speeds are defined as the speeds in the open interval between the shear wave speed and the longitudinal wave speed. For intersonically moving cracks, a ray emanating from the crack tip, representing a line of strong discontinuity (shock), has been observed experimentally (Rosakis et al., 1998; Singh and Shukla, 1996) and predicted theoretically (Liu et al., 1995). Intersonic propagation is achieved under loading conditions that promote locally shear-dominated deformations at the crack tip, which are further enhanced by the stress mismatch resulting from the bimaterial nature of the solid. Experiments have also provided clear evidence of large-scale frictional contact. This contact has subsequently been modeled and analyzed numerically (Huang et al., 1998; Needleman, 1999).

In purely homogeneous materials and in the absence of a weak or prescribed crack growth path, mode-II crack propagation is not possible because the crack spontaneously kinks and subsequently propagates in a direction that induces a local Mode-I state of stress around the tip. This is generally not the case in solids which, while homogeneous (isotropic or anisotropic) as regards their constitutive properties, contain preferred crack paths, e.g., in the form of a weak plane. In these cases, the weak plane may trap the crack, thus allowing for mode-II crack growth. Unidirectional composites provide an additional example of a class of materials which are macroscopically homogeneous but contain preferred crack propagation directions, e.g., in the direction of the fibers, and may therefore support stable mode-II dynamic crack growth.

Rosakis et al. (1999, 2000) investigated the fracture of two identical, weakly bonded, Homalite plates subject to asymmetric impact. The Homalite plates, in addition to being constitutively homogeneous, were also isotropic. The resulting shear cracks, which propagated at speeds between the shear (c_s) and the longitudinal (c_l) wave speeds of the material, featured two clearly discernible shock waves emanating from the crack tip. After accelerating to the longitudinal wave speed of Homalite, the shear cracks settled to a locally steady-state speed slightly above the critical speed $v_c = \sqrt{2}c_s$. The significance of this speed has been revealed by a number of early analytical studies of intersonic crack growth and it will briefly be discussed below.

The first experimental evidence of shear-dominated crack growth along the fibers of a unidirectional composite material has recently been reported by Coker and Rosakis (1998, 2001). In these experiments, the shear fractures were found to propagate at record speeds. Thus, the shear cracks were observed to accelerate to speeds very close to the longitudinal wave speed along the fibers, $c_l = 7400$ m/s, and to subsequently oscillate between this speed and a critical speed $v_c = 6500$ m/s. The experiments also furnished evidence of large-scale frictional contact, in the form of a double-shock wave structure emitted from the crack tip and the end of the traveling contact zone.

Intersonic shear (mode-II) cracks propagating along a weak plane in an otherwise homogeneous (isotropic or anisotropic) solid have been modeled in a number of early analytical studies, long before experimental evidence of the attainability of such phenomena was available. By forcing a shear crack to grow in an isotropic material along a straight path (mathematically equivalent to a weak path or fault), several researchers (Freund, 1979, 1989; Georgiadis, 1986; Broberg, 1989, 1996, 1999) determined analytically the critical speed for intersonic crack growth to be $\sqrt{2}c_s$. For steady crack growth and in the absence of a cohesive crack-tip structure, this is the only speed at which the energy-release rate is nonzero and finite (Broberg, 1996).

Singular asymptotic analyses of intersonic crack growth in anisotropic materials were carried out by Piva and Hasan (1996) and Huang et al. (1999). Shear cracks and dislocations moving intersonically in aniso-

tropic solids have been studied by Gao et al. (1999) in a unified context. As in the isotropic case, these analyses have shown that steady intersonic shear-crack growth in anisotropic materials is possible only at a well-defined intersonic critical speed.

Recently, Broberg (1999) has investigated intersonic crack growth in orthotropic materials in which crack opening obeys a cohesive law. The chief advantage of allowing for cohesive behavior is that a nonzero and finite energy-release rate is predicted over the entire intersonic regime. Broberg's work has additionally shown that the energy-release rate attains a maximum at values close, but not equal, to the critical speed v_c predicted by the singular theory. Moreover, the location of the maximum tends to v_c as the cohesive strength rises to infinity and, correspondingly, the cohesive-zone shrinks to a point.

In the present study, we use a cohesive model of fracture (Camacho and Ortiz, 1996; Ortiz and Pandolfi, 1999; Ruiz et al., 2000, 2001; Pandolfi et al., 1999) in the numerical simulation of the experiments of Coker and Rosakis (1998, 2001). The simulations account for explicit crack nucleation (by a self-adaptive remeshing procedure), crack closure and frictional sliding. We introduce an anisotropic cohesive law, that leads to the nucleation and the propagation of the crack along the fiber direction, consistent with the experimental observations. The behavior of the material is assumed to be rate independent, and, consequently, all rate effects predicted by the calculations are due to inertia, combined with the intrinsic time scale introduced by the cohesive models (Ruiz et al., 2000, 2001). Thus, both the bulk constitutive and the cohesive law properties used in the numerical model are obtained from quasi-static experiments. The objective of the study is twofold. Firstly, the numerical simulations reveal insights into the detailed mechanisms underlying observations such as crack-tip speeds and the emergence of hot spots following the passage of a crack tip. The calculations additionally bear out many of the aforementioned analytical studies and provide useful glimpses into hard-to-observe features such as the temperature distribution in the interior of the specimen. Conversely, the experimental data provides an exacting validation test suite for assessing the fidelity of cohesive models of fracture.

The organization of the paper is as follows. In Section 2, we describe the characteristics of the unidirectional graphite–epoxy composite material. In Section 3 we briefly describe the experimental configuration and the diagnostic techniques employed (Coker and Rosakis, 1998, 2001). In Section 4 we summarize the observations of Coker and Rosakis which provide a basis for the subsequent validation tests. In Section 5 we briefly outline relevant aspects of the finite-element solution procedure. Detailed comparisons between the finite-element simulations and the experimental data are presented in Section 6. The calculations demonstrate the ability of cohesive models of fracture to *predict* salient aspects of the experimental record, such as the crack-tip position and velocity history, the observed double-shock wave structure, the large-scale contact between the crack flanks, and the "hot spots" generated by frictional heating. The effect of the impact speed, cohesive strength and pulse duration is parametrically investigated in Section 6.2.

2. Elastic properties of the graphite–epoxy unidirectional composite

Fig. 1 shows the structure of the graphite–epoxy unidirectional composite tested by Coker and Rosakis (1998, 2001). Fig. 1a shows two cross-sections of the composite plate, normal and parallel to the fibers respectively. In Fig. 1b the orthonormal coordinate set adopted is also shown relative to the fibers. The x_1-axis is chosen to be aligned with fibers and the x_3-axis is perpendicular to the plate. Fiber-reinforced composites are characterized by a strong dependence of the material properties (both constitutive and fracture) on the fibers orientation. The material is stiffer and stronger in the fibers direction; and more compliant and weaker in other directions. In the material under consideration, the fibers are randomly distributed in the epoxy matrix; thus the x_1–x_3 plane can be taken as a plane of isotropy, and the material may be considered transversely isotropic. The elastic constitutive relation is therefore characterized by five independent moduli, and can be written as (Christensen, 1979)

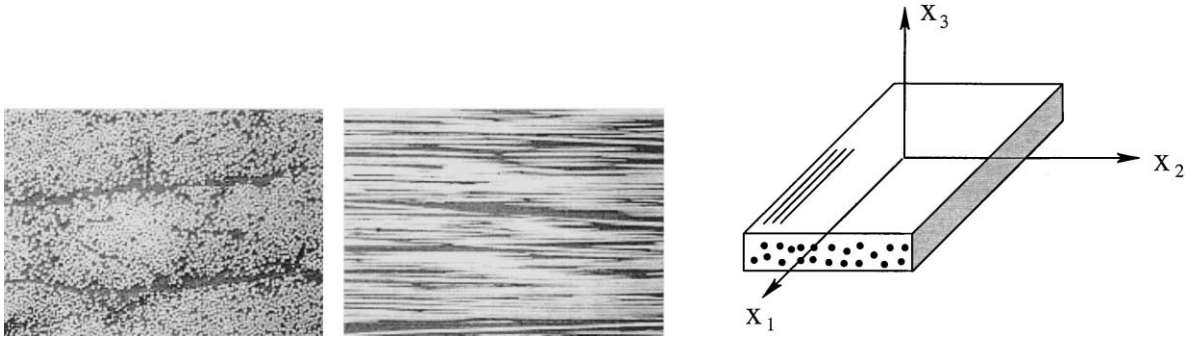

Fig. 1. Cross-sections of fiber-reinforced unidirectional graphite–epoxy composite, in direction parallel and normal to the fibers.

$$\begin{bmatrix} \sigma_1 = \sigma_{11} \\ \sigma_2 = \sigma_{22} \\ \sigma_3 = \sigma_{33} \\ \sigma_4 = \sigma_{23} \\ \sigma_5 = \sigma_{13} \\ \sigma_6 = \sigma_{12} \end{bmatrix} = \begin{bmatrix} c_{11} & c_{12} & c_{12} & 0 & 0 & 0 \\ c_{12} & c_{22} & c_{23} & 0 & 0 & 0 \\ c_{12} & c_{23} & c_{22} & 0 & 0 & 0 \\ 0 & 0 & 0 & (c_{22}-c_{23})/2 & 0 & 0 \\ 0 & 0 & 0 & 0 & c_{66} & 0 \\ 0 & 0 & 0 & 0 & 0 & c_{66} \end{bmatrix} \begin{bmatrix} \varepsilon_1 = \varepsilon_{11} \\ \varepsilon_2 = \varepsilon_{22} \\ \varepsilon_3 = \varepsilon_{33} \\ \varepsilon_4 = \varepsilon_{23} \\ \varepsilon_5 = \varepsilon_{13} \\ \varepsilon_6 = \varepsilon_{12} \end{bmatrix} \tag{1}$$

The elastic moduli are related to the engineering moduli E_1, E_2, μ_{23}, μ_{12} and ν_{12} through the following relations:

$$E_1 = c_{11} - \frac{2c_{12}^2}{c_{22}+c_{23}}, \quad E_2 = \frac{(c_{22}-c_{23})(c_{11}c_{22}+c_{23}c_{11}-2c_{12}^2)}{c_{11}c_{22}-c_{12}^2} \tag{2}$$

$$\mu_{12} = c_{66}, \quad \mu_{23} = \frac{c_{22}-c_{23}}{2} = \frac{E_2}{2(1+\nu_{23})} = c_{44} \tag{3}$$

$$\nu_{12} = \frac{c_{12}}{c_{22}+c_{23}}, \quad \nu_{21} = \frac{c_{12}(c_{22}-c_{23})}{c_{11}c_{22}-c_{12}^2}, \quad \nu_{23} = \frac{c_{23}c_{11}-c_{12}^2}{c_{11}c_{22}-c_{12}^2} \tag{4}$$

For the material under consideration, the shear modulus μ_{12} was determined by a quasi-static Iosipescu shear test, while uniaxial compression tests were conducted on an MTS hydraulic testing machine in order to evaluate the Young moduli, E_1 and E_2, and the Poisson ratio, ν_{12}. The measured values of the elastic moduli are collected in Table 1.

The stiffness coefficients are also related to the plane strain longitudinal and shear wave speeds along the major axes by the following relations:

$$c_1^{\parallel} = \sqrt{\frac{c_{11}}{\rho}}, \quad c_1^{\perp} = \sqrt{\frac{c_{22}}{\rho}}, \quad c_s = \sqrt{\frac{c_{66}}{\rho}} \tag{5}$$

The longitudinal wave speeds parallel $c_1^{\parallel}$ and perpendicular $c_1^{\perp}$ to the fibers and the shear wave speed c_s were obtained using ultrasonic pressure and shear transducers operating at 5 MHz frequency. The average mass density ρ of the composite plate was 1478 kg/m^3. Relations (5) have been used to verify the values of the stiffness coefficients computed by Eqs. (2)–(4). Table 2 reports the measured bulk wave speeds values for plane strain conditions, as well as the Rayleigh wave speed $c_R^{\parallel} = 0.99c_s$, for waves propagating in the fibers direction. In the last column we report the corresponding wave speed values calculated from Eq. (5) under

Table 1
Material properties for the graphite–epoxy unidirectional composite

Coefficient	GPa	Parameter	
c_{11}	82.0	E_1	80.0 GPa
c_{22}	11.1	$E_2 = E_3$	8.9 GPa
c_{12}	4.0	μ_{23}	3.1 GPa
c_{23}	4.9	$\mu_{12} = \mu_{13}$	3.6 GPa
c_{66}	3.6	$\nu_{12} = \nu_{13}$	0.25
c_{44}	3.1	ν_{23}	0.43

Table 2
Characteristic plane strain (measured) and plane stress (calculated) wave speeds for the graphite–epoxy unidirectional composite

Wave type	Plane strain wave speed (m/s)	Plane stress wave speed (m/s)
$c_l^{\parallel}$	7450 ± 100	7380
$c_l^{\perp}$	2740 ± 100	2470
c_s	1560 ± 50	1560
$c_R^{\parallel}$	1548	1548

plane stress condition, i.e., using the reduced stiffness matrix $\boldsymbol{c}'$ obtained through the following relations (Coker and Rosakis, 2001):

$$c'_{11} = c_{11} - \frac{c_{12}^2}{c_{22}}, \quad c'_{22} = c_{22} - \frac{c_{23}^2}{c_{22}}, \quad c'_{12} = c_{12} - \frac{c_{12}c_{23}}{c_{22}}, \quad c'_{66} = c_{66} \tag{6}$$

3. Experimental setup

In the experiments of Coker and Rosakis (1998, 2001) fiber-reinforced epoxy matrix composite plates of dimension 203 mm × 127 mm × 7 mm were used. The specimens comprised 48 plies of graphite fiber in an epoxy matrix. The plates had an edge pre-notch machined in the fibers direction and were loaded by projectile impact in a one-point bend configuration, as shown in Fig. 2. The projectile was fired by a gas-gun, with an impact speed ranging from 10 to 57 m/s. The optical method of coherent gradient sensing (CGS) was used in a reflective arrangement to record the gradient of the out-of-plane displacements on a 50 mm diameter area of the specimen surface, around the crack tip. An infrared high-speed camera measured the temperature field over a 1 mm^2 area on the other side of the plate, at a location close to the pre-notch tip. In the experiments the composite plates were impacted from either the side of the notch, Fig. 2, or the opposite side (not shown in the figure).

The CGS is a full field shearing interferometric technique sensitive to in-plane gradients of the out of plane displacements in reflection mode and to in-plane stress gradients in transmission mode. A detailed description of the technique and of the equations governing optical mapping and fringe formation may be found elsewhere (Tippur et al., 1990, 1991). A schematic of the experimental setup of the CGS optical technique is shown in Fig. 3.

For opaque materials, CGS uses a coherent, monochromatic, collimated laser beam which is shone on, and subsequently reflected by, the optically flat and specularly reflective surface of the specimen. Near the crack tip, the reflected beam acquires an optical path difference due to the deformation of the specimen surface. The reflected beam crosses two high-density line diffraction gratings of pitch $p = 0.0254$ mm (40 lines/mm), normal to x_3 direction, Fig. 3, and separated by a distance Δ. The gratings diffract the reflected

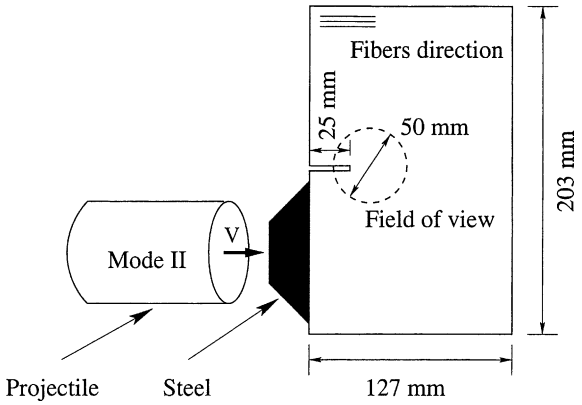

Fig. 2. Single edge notch (SEN) specimen geometry (thickness 7 mm) and size for shear-dominated dynamic fracture experiments.

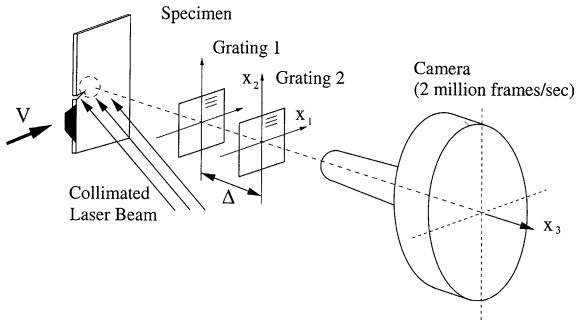

Fig. 3. Schematic of the experimental setup and optical technique of CGS.

beam and recombine it to form an interferogram. The reflected light is collected by a filtering lens, which blocks all but either of the ± 1 diffraction orders. One of those two remaining diffraction spots is imaged to produce an interference pattern on the image plane of a high-speed camera.

When used in reflective mode, CGS measures the in-plane gradients of out-of-plane displacement $u_3(x_1, x_2)$ according to the relation (Tippur et al., 1990, 1991)

$$u_{3,2} = \frac{\partial u_3}{\partial x_2} = \frac{mp}{2\Delta}, \quad m = 0, \pm 1, \pm 2, \ldots \tag{7}$$

where m is the fringe order for the x_2 gradient contours. Eq. (7) holds when the lines of gratings are parallel to x_1 direction. Each CGS fringe is a locus of points of constant $u_{3,2}$ on the specimen surface. Under plane-stress linear-elastic conditions, $u_3(x_1, x_2)$ is related to the average stresses across the thickness as follows (Lambros and Rosakis, 1995b; Liu et al., 1998):

$$u_3 = \frac{h}{2}(b_{31}\sigma_{11} + b_{32}\sigma_{22}) \tag{8}$$

where h is the specimen thickness and b_{ij} are components of the compliance matrix, inverse to the elastic moduli matrix in Eq. (1).

On the opposite side of the plate, and simultaneously with the CGS measurements, a full-field, high-speed infrared imaging system, Fig. 4, was employed to measure the evolving, two-dimensional temperature

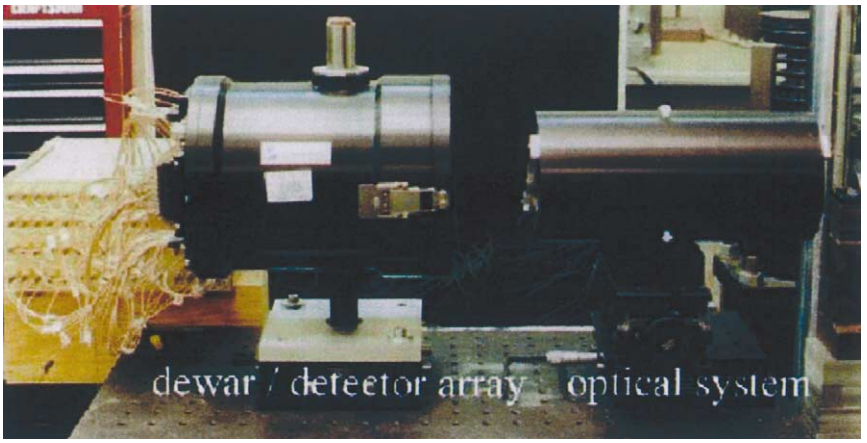

Fig. 4. The infrared high-speed camera.

field along the crack path. The thermal camera is designed to capture full-field images at a rate of 10^6 frames per second with a system rise time of 750 ns (Zehnder et al., 2000). An essential component of the system is an 8×8 focal-plane array of HgCdTe IR detector elements. Each detector element is 100 mm $\times$ 100 mm in size, with center-to-center spacing of 130 mm. The detectors are housed in a liquid nitrogen dewar and are operated at a temperature of 77 K to maximize the signal-to-noise ratio. The camera is focused on 1.1 mm $\times$ 1.1 mm area ahead of the notch tip. Radiation emitted from the object as it deforms and heats up is focused onto the IR focal plane array. A calibration curve for the graphite–epoxy composite used in the tests was obtained which enabled the conversion of voltage signals to temperatures.

4. Experimental observations

A sequence of six CGS interferograms, corresponding to shear-dominated dynamic crack growth along the fibers, is shown in Fig. 5 (Coker and Rosakis, 1998, 2001). As the dynamic shear crack initiates and propagates directly ahead of the initial pre-notch, it accelerates and a marked change can be observed in the shapes of the crack-tip fringe patterns. Thus, the rear fringe loop shape changes from rounded (see first three frames) to a triangular wedge, bounded by a line of highly concentrated fringes emerging from the crack tip at a well-defined angle (see Fig. 5, last three frames). This line is caused by a steep change in the stress gradients in a localized area, which, as the crack exceeds the shear wave speed, forms a stress discontinuity or shock (Liu et al., 1995; Rosakis et al., 1998; Huang et al., 1999). Finally this line broadens into two parallel lines (a double-shock wave) which intercept the crack surfaces over a finite area of about 4–5 mm behind the crack tip.

One possible reason for the observed double-shock structure may be the existence of a finite size contact region behind the crack tip. A similar phenomenon of large-scale contact during intersonic crack growth in bimaterials was reported by Lambros and Rosakis (1995a), and numerically simulated by Needleman and Rosakis (1999). The presence of the contact region in the graphite–epoxy composite experiments is strongly supported by the two-dimensional high-speed infrared camera images (presented in this paper for the first time). Infrared thermal images are shown in Fig. 6 for one of the shear crack growth experiments. The camera is focused on the square area (1.1 mm $\times$ 1.1 mm) ahead of the notch tip as shown in the top-left

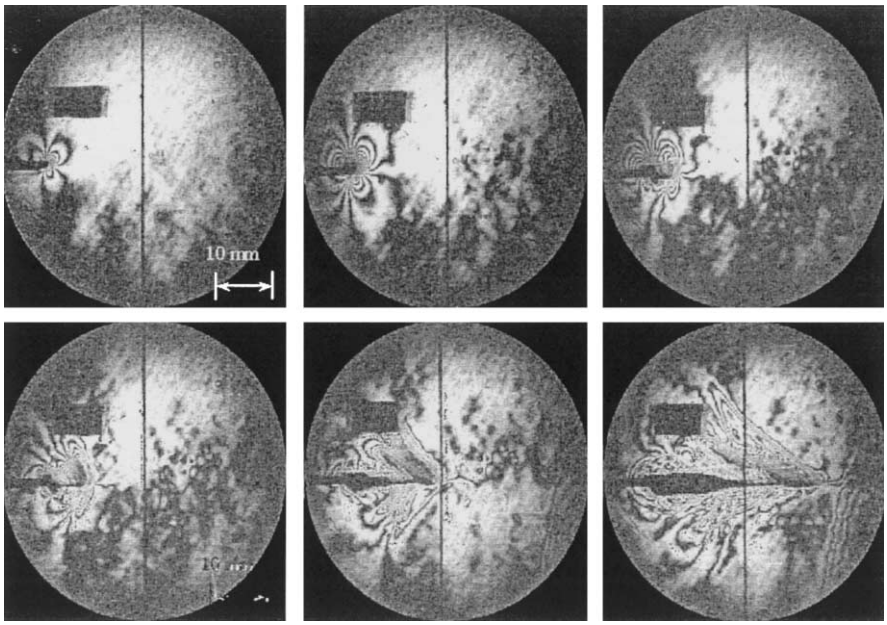

Fig. 5. Experimental observations: sequence of CGS interferograms showing intersonic crack tip at times 2.8, 4.2, 5.6, 6.9, 8.3, 9.7 μs. The field of view is a 50 mm diameter circle around the pre-notch tip (Coker and Rosakis, 1998, 2001).

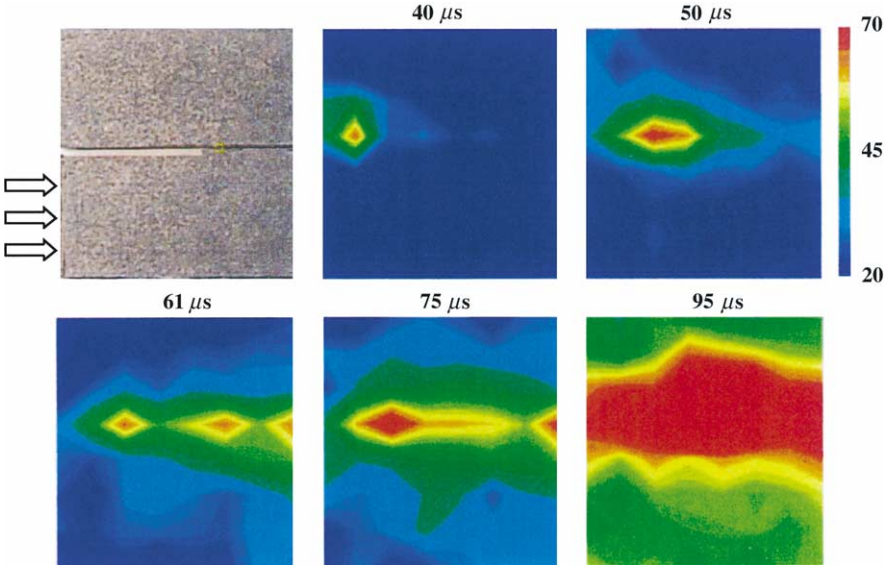

Fig. 6. Experimental observations: high-speed infrared images of hot spot formation due to contact behind an intersonically moving shear crack. The top-left image shows the size of the exposed area (1.1 mm × 1.1 mm square ahead of the crack tip). The following images show contours of constant temperature at different time steps.

image of Fig. 6. The following images in Fig. 6 show contours of constant temperature elevation at subsequent times. Local hot spots are observed to form along the fracture surfaces due to frictional contact.

Hot spots appear firstly after the crack completely crossed the specimen width, and in the initial stages their position shifts frequently in time. It seems evident that the wave reflection between the plate edges helps the intermittent frictional contact between the two fracture surfaces. The high-temperature region is initially localized to the crack surfaces and subsequently grows in width, until it finally saturates the infrared detectors. It should be carefully noted that the measured temperatures represent averages over a 100 μm × 100 μm area, and thus are likely to be lower than the actual peak temperatures.

The instantaneous crack-tip position can be recovered from the frames recorded by the high-speed camera. For each experiment it is possible to determine the crack length and, by numerical differentiation of the crack-tip record, the crack-tip speed history. It bears emphasis that in all the experiments the crack-tip speed exceeded the shear-wave speed and was clearly intersonic (Coker and Rosakis, 1998, 2001), with average values close to 6000 m/s. The elastic asymptotic field analysis of Huang et al. (1999) gives the following expression for the critical crack-tip speed v_c:

$$v_c = c_s \sqrt{\frac{E_1}{\mu_{12}(1+\nu_{12})}} \tag{9}$$

For the graphite–epoxy composite material properties reported above, Eq. (9) gives $v_c = 6327$ m/s, which, allowing for the experimental error inherent in the determination of crack-tip speeds, is in remarkable agreement with experiment (Coker and Rosakis, 1998, 2001). It is also noteworthy that the highest measured crack-tip speed was 7400 m/s, which is, within experimental error, ostensibly equal to the longitudinal wave speed c_l in the fibers direction. To the best of our knowledge, this is the highest crack-tip speed ever observed in a laboratory setting or ever reported in the open literature.

5. Anisotropic cohesive model

Our calculations employ the cohesive model proposed by Camacho and Ortiz (1996), and subsequently extended to three dimensions by Ortiz and Pandolfi (1999), in order to simulate crack initiation and growth. In the present work, these models are extended so as to account for the anisotropy induced by the reinforcing fibers in the fracture properties of the composite.

In adopting a cohesive description of fracture, the formation of a crack is regarded as a gradual process of separation, either by opening or by shearing, leading to the formation of new free surfaces. The cohesive law furnishes the traction vector $\boldsymbol{t}$ across the cohesive surface as a function of the opening displacement $\boldsymbol{\delta} = [\![\boldsymbol{u}]\!]$. Following Camacho and Ortiz (1996), this cohesive behavior is formulated in terms of the effective opening displacement

$$\delta = \sqrt{\beta^2 \delta_S^2 + \delta_n^2} \tag{10}$$

where

$$\delta_n = \boldsymbol{\delta} \cdot \boldsymbol{n} \tag{11}$$

is the normal component of the opening displacement and

$$\delta_S = |\boldsymbol{\delta} - \delta_n \boldsymbol{n}| \tag{12}$$

is the magnitude of the tangential opening displacement, Fig. 7. The cohesive behavior under monotonic loading is then assumed to be governed by a cohesive potential $\phi(\delta)$. The resulting tractions are of the form

$$\boldsymbol{t} = \frac{\partial \phi}{\partial \boldsymbol{\delta}} = \frac{t}{\delta}(\beta^2 \boldsymbol{\delta}_S + \delta_n \boldsymbol{n}) \tag{13}$$

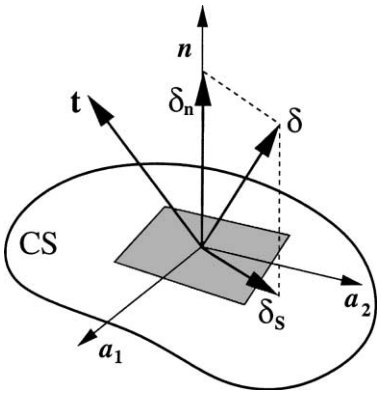

Fig. 7. Decomposition of the opening displacement into normal and tangential components.

where

$$t = \sqrt{\beta^{-2}|\boldsymbol{t}_S|^2 + t_n^2} \tag{14}$$

is an effective cohesive traction,

$$t_n = \boldsymbol{t} \cdot \boldsymbol{n} \tag{15}$$

is the normal component of the cohesive traction and

$$t_S = |\boldsymbol{t} - t_n \boldsymbol{n}| \tag{16}$$

is the magnitude of the tangential opening displacement. It follows from Eq. (14) that the parameter β measures the ratio of shear and normal cohesive strength of the material. It also roughly defines the ratio of K_{IIc} to K_{Ic} of the material (Ruiz et al., 2000). The particular monotonic envelop adopted in calculations is shown in Fig. 8. Thus, potential cohesive surfaces are assumed to be rigid up to the attainment of the cohesive strength σ_c, and the effective cohesive traction to subsequently decrease linearly and vanish upon the attainment of a critical effective opening displacement δ_c. The resulting fracture energy of the material is $G_c = \sigma_c \delta_c / 2$ (Ortiz and Pandolfi, 1999). The cohesive element is rendered irreversible by unloading to the origin from the monotonic envelop just described, Fig. 8 (Camacho and Ortiz, 1996).

It is interesting to note that our numerical model is fully rate independent, i.e., the bulk constitutive law and the cohesive law are fed with quasi-static mechanical parameters only. Thus, all the rate effects predicted by the calculations are a consequence of inertia combined with the characteristic time of cohesive models (Camacho and Ortiz, 1996).

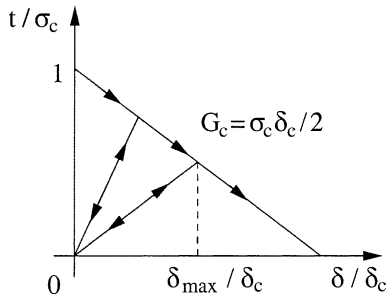

Fig. 8. Linearly decreasing monotonic envelop and loading/unloading rule.

It bear emphasis that upon closure, the cohesive surfaces are subjected to the contact unilateral constraint, including friction. We regard contact and friction as independent phenomena to be modeled outside the cohesive law. In Eqs. (10)–(16) δ_n is assumed equal to zero if negative (crack flanks closure), and a suitable contact law is activated.

The unidirectional structure of fiber-reinforced composites induces a marked anisotropy in their fracture properties. Thus, these composites are designed so as to increase the strength of the matrix material in the direction of the fibers, while the strength parallel to the fibers remains ostensible identical to that of the matrix. In consequence, the toughness of the material attains a maximum when the crack plane is normal to the fibers, and it attains a minimum when the crack plane contains the direction of the fibers. This orientation dependence of the toughness of fiber-reinforced composites has been analyzed by Allix and Ladeveze (1992), Corigliano (1993) and Allix et al. (1995). In the present work, we model fracture anisotropy as a dependence of the cohesive strength $\sigma_c(\boldsymbol{n})$ on the normal $\boldsymbol{n}$ to the crack plane. Assuming that this dependence is quadratic and invariant upon reflection of $\boldsymbol{n}$ to $-\boldsymbol{n}$ we further have

$$\sigma_c(\boldsymbol{n}) = \Sigma_{ij} n_i n_j \tag{17}$$

where the tensor Σ_{ij} is a material property. In particular, fiber-reinforced composites are transversely isotropic in the direction of the fibers. Taking this symmetry into account, Eq. (17) reduces to

$$\sigma_c(\boldsymbol{n}) = \sigma_{c\,\min} + (\sigma_{c\,\max} - \sigma_{c\,\min}) \cos^2 \alpha \tag{18}$$

where α is the angle between $\boldsymbol{n}$ and the direction of the fibers, $\sigma_{c\,\max}$ denotes the maximum cohesive strength normal to the fibers, and $\sigma_{c\,\min}$ denotes the minimum cohesive strength parallel to the fibers. The fracture properties of the graphite–epoxy material used in calculations are collected in Table 3. The ratio between maximum and minimum cohesive strength has not been directly measured.

In order to gain some understanding of the hot-spots which are observed to develop behind the crack tip, we additionally account for crack closure and for Coulomb friction between the crack flanks. These effects are modeled by means of the friction algorithm proposed by Giannakopoulos (1989). This algorithm introduces a slight surface compliance into Coulomb's law and updates the traction vector by a nonassociated return mapping algorithm. The temperature rise in the contact area is estimated through the relation

$$T = T_0 + \frac{F}{\rho C_v L} \tag{19}$$

where T_0 is the initial temperature, ρ is the mass density, C_v is the heat capacity, L is a characteristic width of the initial thermal layer, and

$$F = \boldsymbol{t} \cdot [\![\boldsymbol{u}]\!] \tag{20}$$

is the work of friction. Thus we assume that, initially, the entire work of friction is converted into heat within a small boundary layer of thickness L, which accounts for the fracture surface asperities. This model is aimed at describing the observed short-term response of the specimen, including the development of hot spots. The longer term evolution of the temperature field, which involves heat conduction, is not accounted

Table 3
Fracture properties of the graphite–epoxy unidirectional composite used in calculations

Fracture toughness normal to the fiber	$K_{Ic\,\min}$	2.2 MPa$\sqrt{\text{m}}$
Fracture energy normal to the fiber	$G_{Ic\,\min}$	474.0 N/m
Cohesive strength normal to the fiber	$\sigma_{c\,\min}$	35.8 MPa
Maximum/minimum cohesive strength ratio	$\sigma_{c\,\max}/\sigma_{c\,\min}$	100
Shear/normal strength ratio	$\beta = \tau_c/\sigma_c$	0.726
Critical opening displacement	δ_c	0.0265 mm

Table 4
Frictional and thermal parameters used in calculations

Friction coefficient	f_C	0.7
Heat capacity	C_v	1170 J/kg K
Thermal layer thickness	L	0.003 mm

for in the analysis. The numerical values of the frictional and thermal parameters used in calculations are collected in Table 4.

6. Numerical results

The experimental observations described in the foregoing provide a rich data set for the validation of cohesive models of fracture. Conversely, the detailed simulation of the experiments of Coker and Rosakis (1998, 2001) presented in this section provide useful insights into the mechanisms underlying the observed behavior. All calculations are carried out using explicit dynamics, thus the time step is upper-bounded by stability (Hughes, 1983). The effect of the projectile impact, smoothed by the presence of a steel plate, is approximated by prescribing a velocity profile over the contact area, Fig. 9. The impulse duration t_p is taken to be 27.3 μs; both the rise time t_r and the ramp-down time t_d are 2 μs. The plateau extension is defined by the mass and the length of the projectile. For simplicity, the duration of the ramp-down time has been taken equal to the rise time. Observe that the tail extension of the velocity profile does not affect the numerical analysis, since the crack crosses the entire width of the specimen in 22.2 μs. The impact velocity in the numerical analyses is assumed to be 30 m/s, unless differently stated.

The particular class of cohesive elements used in calculations consists of two six-node triangles endowed with quadratic displacement interpolation (Ortiz and Pandolfi, 1999), Fig. 10. Further details of the formulation can be found in Ortiz and Pandolfi (1999). Following Camacho and Ortiz (1996), we adaptively create new surfaces as required by the cohesive model by duplicating nodes along previously coherent volume elements interfaces and inserting a new cohesive element. We insert a cohesive element when the effective traction acting on an element interface reaches the cohesive strength of the interface, i.e., when

$$t \geqslant \sigma_c(\boldsymbol{n}) \tag{21}$$

where t is given by (13), $\boldsymbol{n}$ is the normal to the interface and, for the fiber-reinforced composites under consideration here, $\sigma_c(\boldsymbol{n})$ is given by (18). An efficient implementation of the cohesive element insertion procedure may be found in Pandolfi and Ortiz (1998, 2002).

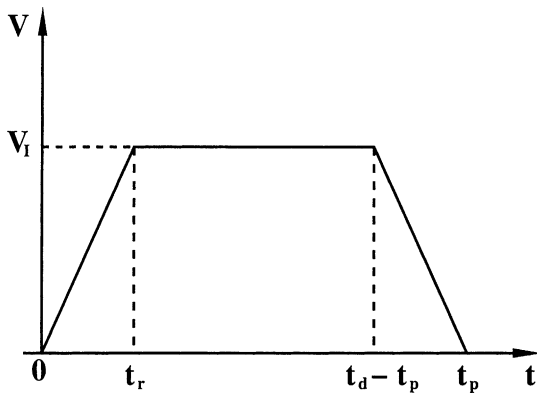

Fig. 9. Impact velocity profile adopted in the simulations.

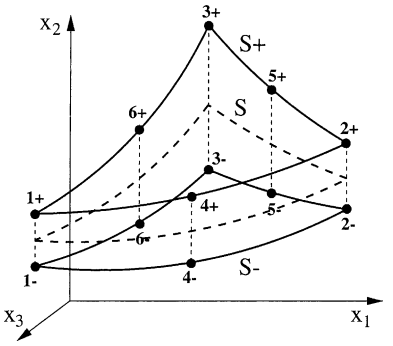

Fig. 10. Geometry of cohesive element. The surfaces S^- and S^+ coincide in the reference configuration of the solid.

The specimen is discretized into ten-node quadratic tetrahedral elements. We employ two meshes: a coarse mesh comprising 5465 nodes and 2666 elements, Fig. 11a; and a fine mesh which comprises 44,593 nodes and 24,685 elements, Fig. 11b. The minimum mesh size $h_{\min} = 2.15$ mm in the coarse mesh is chosen so as to resolve the characteristic cohesive zone size, which may be estimated as (Dugdale, 1960; Barenblatt, 1962; Rice, 1968)

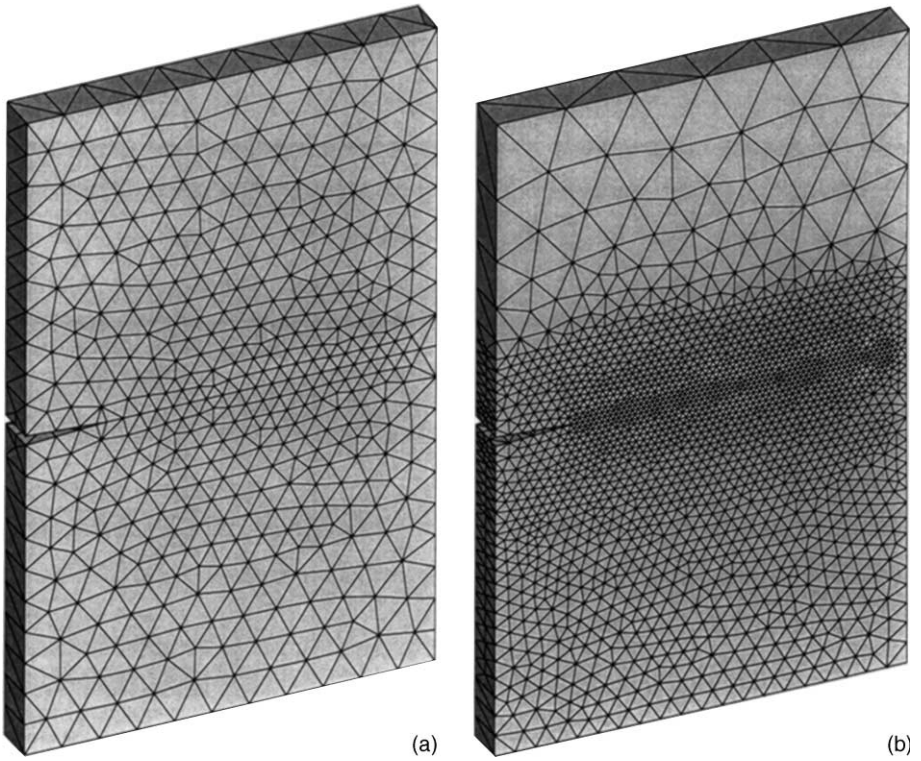

Fig. 11. Computational meshes. (a) Coarse mesh, $h_{\min} = 2.15$ mm, 5465 nodes, 2666 elements. (b) Fine mesh, $h_{\min} = 0.5$ mm, comprising 44,593 nodes and 24,685 elements.

$$R = \frac{\pi E G_c}{8(1-\nu^2)\sigma_0^2} \tag{22}$$

where $E = E_2$ is the Young modulus, $\nu = \nu_{12}$ the Poisson ratio, G_c the specific fracture energy, and σ_0 represents an average cohesive traction. For the assumed linearly decreasing cohesive envelop, $\sigma_0 = 0.5\sigma_c$, and the corresponding cohesive zone size is $R = 5.5$ mm, which is indeed resolved by the coarse mesh. The minimum mesh size in the fine mesh is $h_{\min} \sim 0.5$ mm. The corresponding stable time steps (Hughes, 1983) adopted in the calculations are 0.024 μs for the coarse mesh and 0.0056 μs for the fine mesh.

6.1. Crack-tip speed

Fig. 12 shows a comparison between experimentally observed and computed crack-tip speeds as a function of crack extension. For consistency, the same numerical differentiation scheme for calculating the crack speed was applied to the experimental data and the computed results. The experimental data suggests that the crack accelerates following initiation and attains intersonic speeds, lying between the Rayleigh and the shear wave speeds of the material, after an extension of about 35 mm. These features are closely captured by the numerical calculations. It is interesting to note that the calculated crack-tip speed vs position relation is relatively insensitive to the mesh size. In particular, the discrepancy in the curves resulting from the coarse and fine meshes is within experimental error.

Four successive snapshots of the numerical contour levels of the normal stress component σ_{22} are shown in Fig. 13. The first snapshot shows the initial compressive wave induced by the impact, as it travels the width of the lower half of the specimen. In subsequent snapshots a double-shock wave structure becomes clearly evident. A direct comparison between the calculated shock wave structure around the crack tip and the corresponding experimental CGS fringes at time 18.6 μs is given in Fig. 14. The close agreement between the two images is remarkable. The swept-back double-shock structure of the near-tip fields is strongly suggestive of intersonic crack growth and frictional contact between the crack flanks, and is in accordance with the existing asymptotic solutions (Freund, 1979; Huang et al., 1999; Gao et al., 1999). A close inspection of the crack-face regions in the experimental and numerical images reveals a string of local fringe concentrations, which is suggestive of intermittent frictional interactions between the crack flanks.

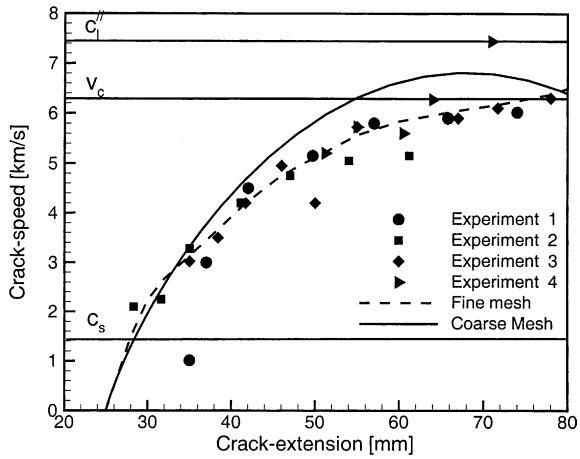

Fig. 12. Crack-tip speed vs crack-tip position: comparison between experiments (Coker and Rosakis, 1998, 2001) (symbols) and numerical results (lines). The crack-tip velocity clearly reaches intersonic values lying between the shear and the longitudinal wave speed.

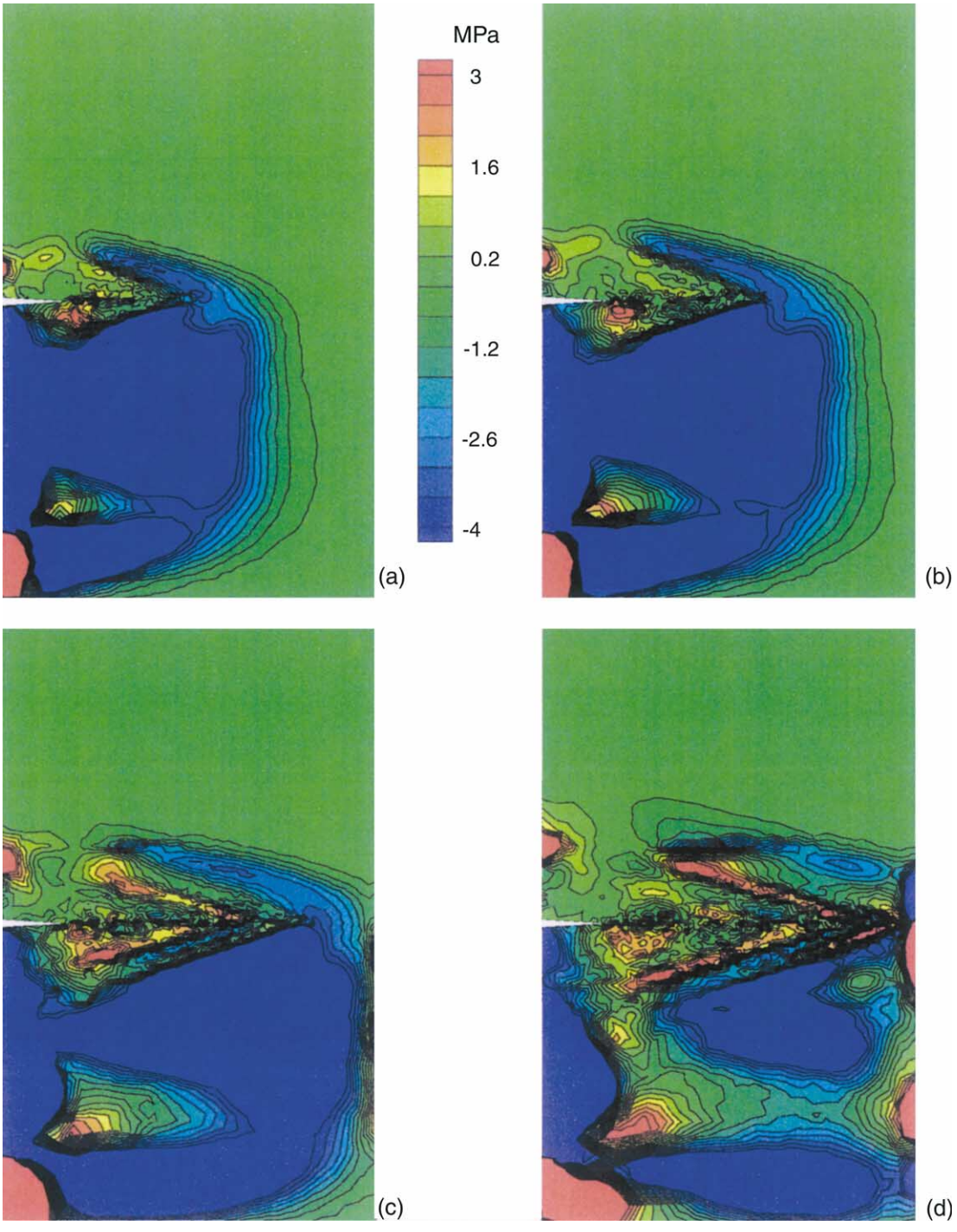

Fig. 13. Numerically computed contour levels of σ_{22} at times: (a) 10.8 μs; (b) 14.4 μs; (c) 18.6 μs; (d) 22.2 μs.

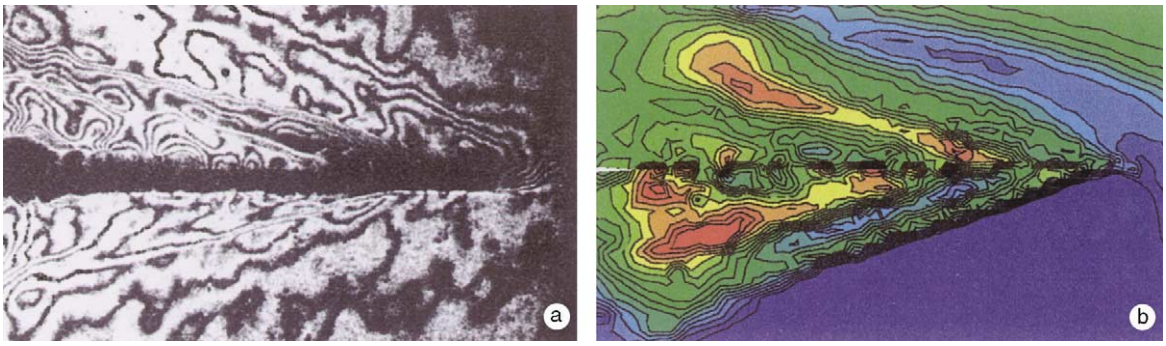

Fig. 14. Comparison between (a) experimental (Coker and Rosakis, 1998, 2001) and (b) numerical shock wave structure. The color scale in the numerical contour plot in (b) agrees with the legend in Fig. 13.

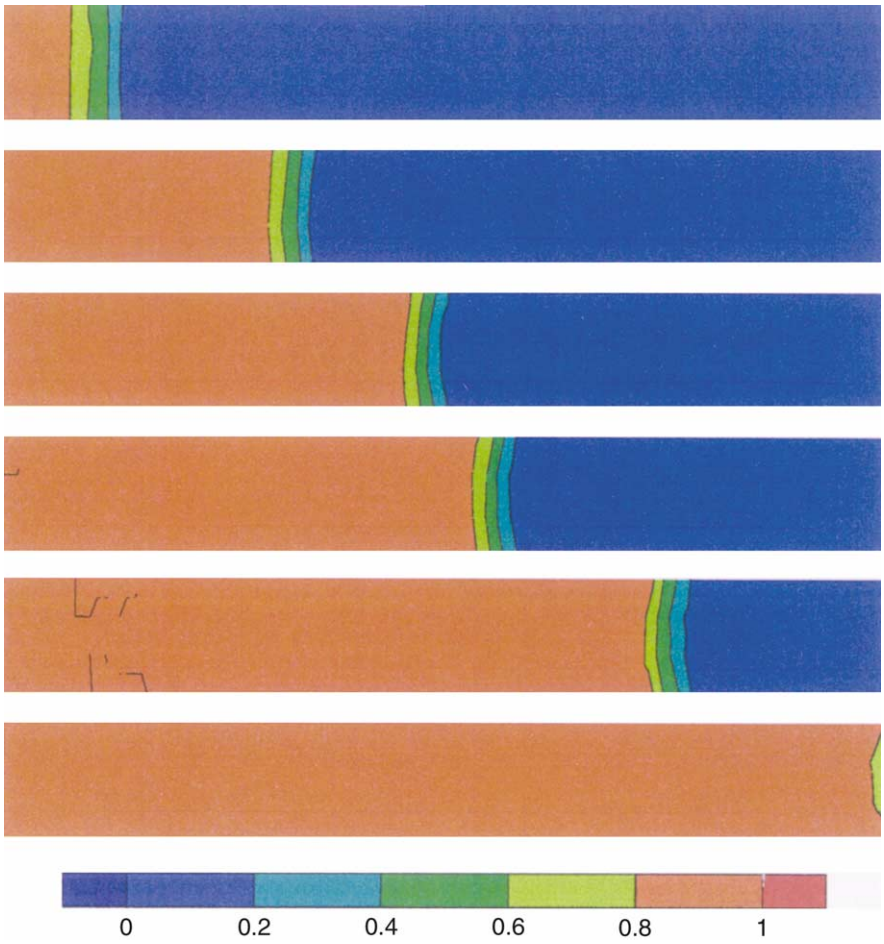

Fig. 15. Numerical contour levels of the damage variable at time 9.6, 12, 13.2, 15.6, 18.6 and 22.2 μs.

Fig. 15 shows the evolution of the crack front within the crack plane, as obtained in the numerical calculations. The plot depicts contours of damage, defined as the ratio D of the spent to total fracture

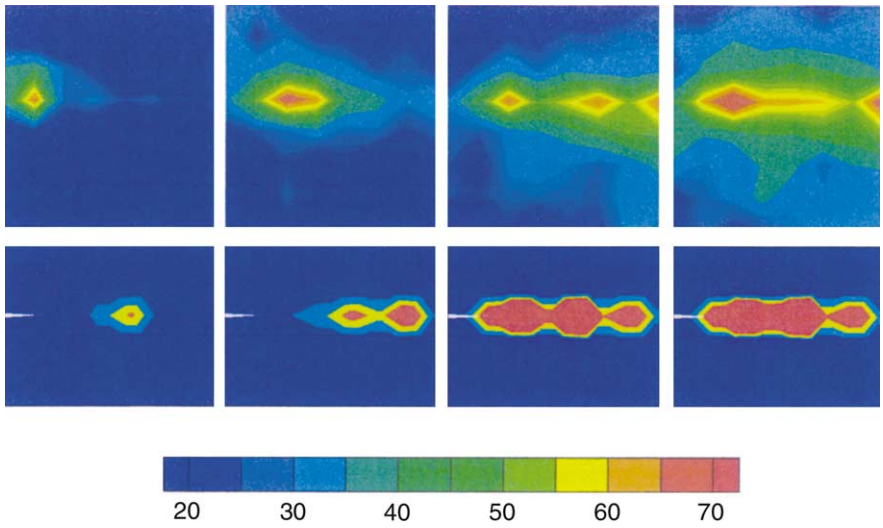

Fig. 16. Comparison of experimental (top) and numerical (bottom) temperature values. Experimental images are taken at times 40, 50, 61 and 75 μs. Numerical images are taken at times 40, 50, 60 and 70 μs.

energy per unit surface. With this definition, the damage variable is dimensionless and ranges from 0, corresponding to an intact surface, to 1, corresponding to a fully crack surface. The transition zone wherein the damage variable takes intermediate values may be regarded as the cohesive zone, and the crack front may conventionally be identified with the level contour $D = 1/2$. It is interesting to note that the crack front is concave in the direction of propagation, a feature which is characteristic of mode-II crack growth. Thus, in marked contrast to mode-I cracks, the interior of the crack front ostensibly lags behind the points of intersection with the lateral surfaces. At about 22.2 μs after impact the crack has swept through the entire width of the specimen.

As already mentioned, the double-shock structure of the near-tip field and the string of trailing 'shocklets' are suggestive of intermittent frictional interactions between the crack flanks. One manifestation of this intermittent friction is the experimentally observed 'hot spots' alluded to in Section 4. Selected frames recorded by the infrared camera are collected in Fig. 16a, and are compared to the corresponding calculated frames in Fig. 16b. Interestingly, both sets of frames show a string of surface hot spots which arise following the passage of the crack tip. The observed and computed hot-spot structures agree both in geometry as well as in the magnitude of the temperature elevation. The analysis thus suggests intermittent friction as the origin of the experimentally observed hot spots. Fig. 17 additionally depicts the computed through-thickness variation of the crack-flank temperature field. It is interesting to note that the hot spots arise near the surface, which suggests that most of the frictional contact occurs in that region. The hot-spot patterns on either side of the specimen are quite dissimilar, which underscores the three-dimensional nature of the frictional interactions and, more generally, of shear-crack growth.

6.2. Parametric studies

We conclude this section by presenting parametric studies on the effect of the impulse time, fracture energy and cohesive strength σ_c on the crack-tip length and velocity histories.

Fig. 18 depicts the crack-speed history at an impact speed of 50 m/s, a cohesive strength of 35.8 MPa and impact durations ranging from 2.5 to 31 μs. As may be observed in the figure, the impulse duration has a

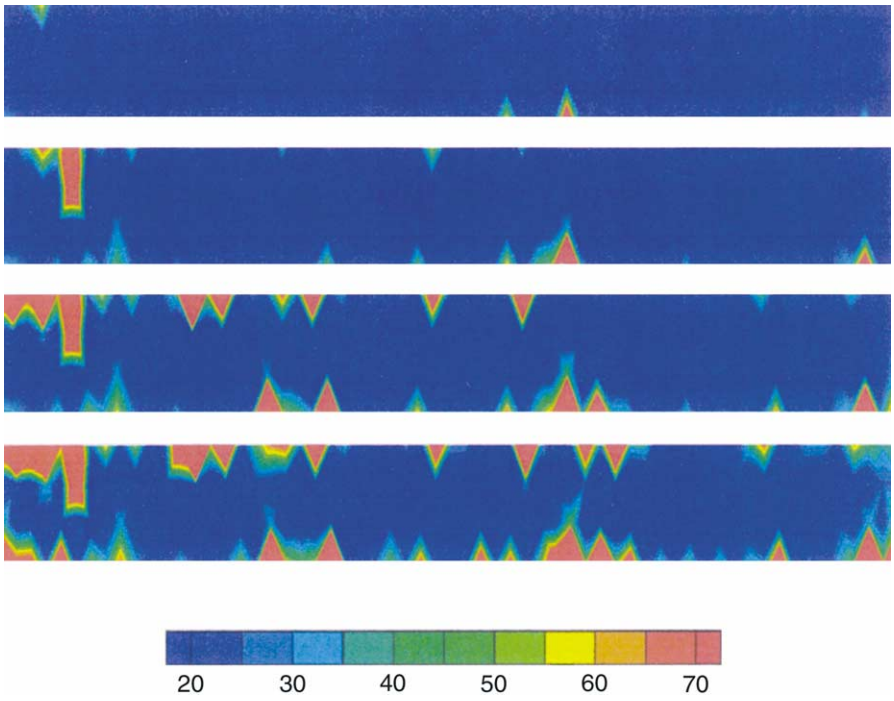

Fig. 17. Numerical temperature distribution across the crack surface at time 40, 50, 60 and 70 μs.

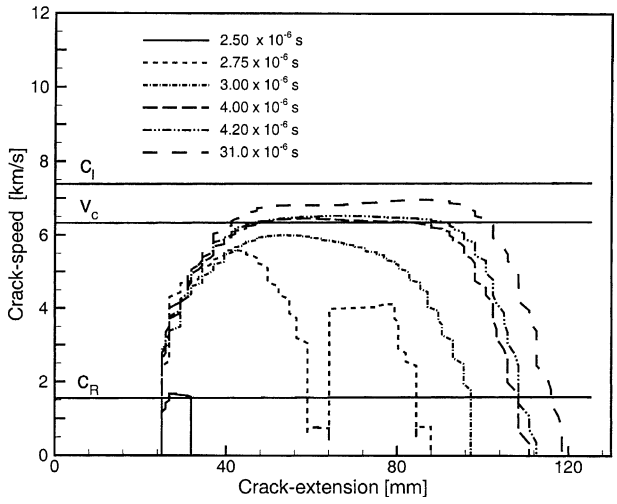

Fig. 18. Parametric study. Crack-speed history as a function of crack tip location at different impact durations. The impact speed is 50 m/s.

marked effect on the crack-tip speed history and the maximum attained crack-tip speed. For an impulse duration in excess of 4 μs, the crack reaches the critical speed v_c and propagates stably at this speed through most of the width of the specimen. For an impact duration of 2.5 μs, the crack accelerates to the Rayleigh

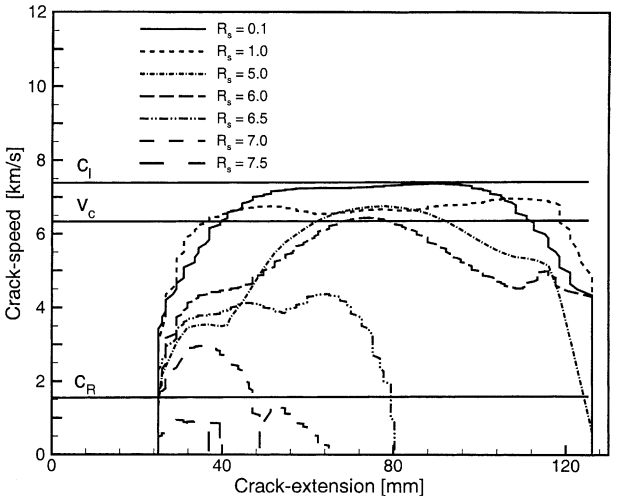

Fig. 19. Parametric study. Crack-speed history as a function of fracture energy. The parameter R_s^2 is the ratio between the fracture energy used in the calculations and the measured value. The cohesive strength σ_c and critical opening displacement δ_c are both scaled by the same factor R_s. The impact speed is 30 m/s and impulse duration is 31 μs.

wave speed and subsequently arrests permanently after some crack advance. For an impact duration of 2.75 μs the crack-tip speed appears to vacillate between two values above and below the Rayleigh wave speed before eventually arresting.

We have also investigated the effect of fracture energy on crack-tip speed. In order to vary the fracture energy, we apply a common scaling factor R_s in the range 0.1–7.5 to the cohesive strength σ_c and the critical opening displacement δ_c, with the result that the fracture energy G_c is scaled by R_s^2. A ratio $R_s = 1$ corresponds to the measured value of the fracture energy. In all calculations, the impulse duration is kept at 31 μs and the impact speed at 30 m/s. Fig. 19 shows the computed crack-tip histories. The main effect of an increase (decrease) in fracture energy is to retard (anticipate) the crack-growth initiation time, and to reduce (increase) the maximum propagation speed. For the highest value of the fracture energy the crack-tip speed remains below the Rayleigh wave speed and the crack arrests shortly after initiation. It is particularly noteworthy that for a sufficiently small fracture energy the crack speed attains values in the vicinity of the longitudinal wave speed, in keeping with the observations of Needleman (1999). For fracture energies corresponding to R_s in the range of 1–6 the crack-tip speed attains the critical value v_c. For intermediate fracture energies corresponding to ratios $R_s = 6.5$ and 7.0, the maximum crack-tip speed exceeds the Rayleigh wave speed by remains below v_c. The higher fracture energies result in intermittent crack growth, with alternating growth and arrest phases.

Fig. 20 shows the effect of impact velocity on crack propagation. In all cases, the impulse duration is held at 31 μs and the cohesive strength at 35.8 MPa, while the impact velocity ranges from 10 to 200 m/s. For impact velocities in the range of 20–50 m/s, the crack tip rapidly reaches the critical speed v_c and subsequently propagates at nearly constant speed. For impact velocities of 100 and 200 m/s, the maximum crack-tip speed approaches or attains the longitudinal wave speed $c_l = 7450$ m/s.

Finally, in Fig. 21 we plot the minimum value of the impact speed required in order to attain the critical crack-tip speed v_c as a function of impulse duration. In all calculations, the cohesive strength is held constant at $\sigma_c = 35.8$ MPa. The attainment of the critical speed depends sensitively on the supply of energy, which is controlled by experimental parameters such as the impact speed or the impulse duration. The impulse duration is in turn a function of the length and mass of the projectile. The trend exhibited in Fig. 21

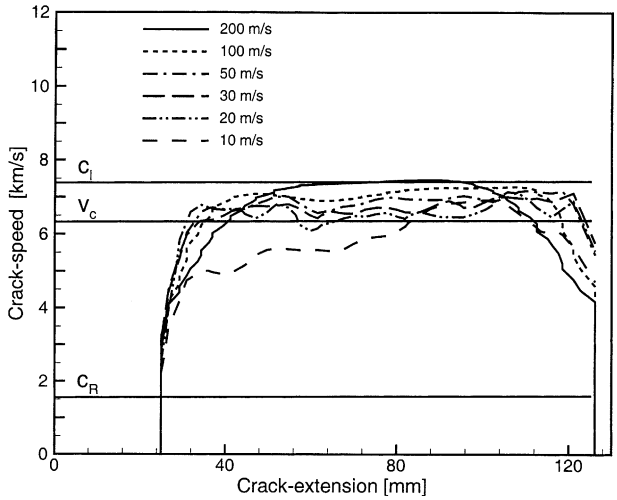

Fig. 20. Parametric study. Crack-speed history at different impact speeds. The cohesive strength is held at 35.8 MPa and the impulse duration at 31 μs.

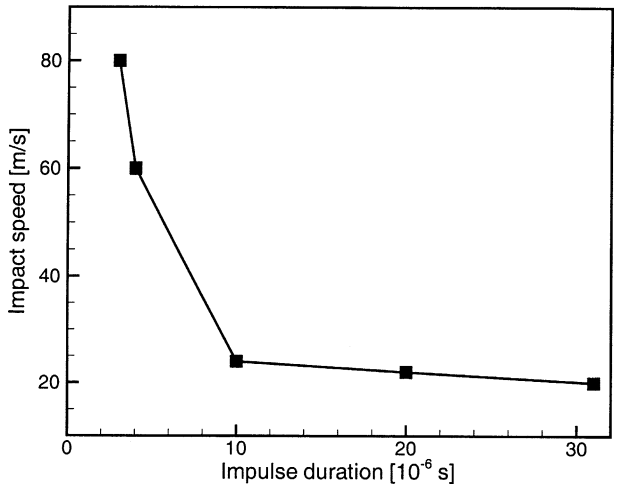

Fig. 21. Numerical evaluation of the minimum impact velocity required in order to attain the critical crack-tip speed v_c as a function of impulse duration. The cohesive strength is $\sigma_c = 35.8$ MPa.

is qualitatively similar to the predictions of Needleman and Rosakis (1999) for intersonic crack growth in metal/polymer bimaterials.

7. Summary and conclusions

We have used an anisotropic cohesive model of fracture to simulate Coker and Rosakis' experiments (1998, 2001), where intersonic shear-dominated crack growth in unidirectional graphite–epoxy composites was observed. The simulations account for explicit anisotropic crack nucleation, crack closure and fric-

tional sliding. The parameters used in the numerical models for the bulk constitutive and cohesive laws were obtained from quasi-static experiments. The behavior of the material is assumed to be rate independent and, consequently, all rate effects predicted by the calculations are due to inertia and to the intrinsic time scale typical of cohesive models (Ruiz et al., 2000, 2001).

The numerical results clearly capture the state of stress around the propagating crack, including the double-shock structure, the crack speed regimes and surface hot spots observed behind the crack in the experiments.

The intersonic crack speed regimes revealed by the simulations presented here are consistent with the analyses of Huang et al. (1999) and Gao et al. (1999). Thus, the calculations suggest that, provided that sufficient energy is supplied to the crack tip, the critical speed v_c is a preferred crack-tip speed for locally steady-state growth of dynamic shear cracks. The special significance conferred to the critical speed v_c by the analytical studies of Huang et al. (1999) and Gao et al. (1999) is amply born out by our numerical calculations. If the crack is driven hard enough, it becomes possible to for the crack tip to attain speeds in the vicinity of the longitudinal wave speed in the direction of the fibers, in keeping with the observations of Needleman (1999).

The calculations also predict a double-shock which emanates from a finite size contact region behind the crack tip. A similar phenomenon of large-scale contact during intersonic crack growth in bimaterials was reported by Lambros and Rosakis (1995a) and numerically simulated by Needleman and Rosakis (1999). The predicted double-shock structure of the near-tip fields is in close agreement with the experimental observations. The calculations additionally predict the presence of a string of surface hot spots which arise following the passage of the crack tip. The observed and computed hot-spot structures agree both in geometry as well as in the magnitude of the temperature elevation. The analysis thus suggests intermittent friction as the origin of the experimentally observed hot spots.

Finally, the parametric study permits to evaluate the influence of experimental parameters as impact speed and impulse duration on the attainment of the critical speed v_c. The trend exhibited by the numerical results is qualitatively similar to the prediction of Needleman and Rosakis (1999).

Acknowledgements

AJR and DC acknowledge the support of the Office of Naval Research through grant N00014-95 to Caltech and the support of the National Science Foundation grant CMS9813100. CY, AP and MO are grateful for DoE support provided through Caltech's ASCI/ASAP Center for the Simulation of the Dynamic Response of Solids.

References

Allix, O., Ladeveze, P., 1992. Interlaminar interface modelling for the prediction of laminates delamination. Composite Structures 22, 235–242.

Allix, O., Ladeveze, P., Corigliano, A., 1995. Damage analysis of interlaminar fracture specimens. Composite Structures 31, 61–74.

Barenblatt, G.I., 1962. The mathematical theory of equilibrium of cracks in brittle fracture. Advances in Applied Mechanics 7+ , 55–129.

Broberg, K.B., 1989. The near tip field at high crack tip velocities. International Journal of Fracture 39, 1–13.

Broberg, K.B., 1996. How fast can a crack go? Materials Science 32 (1), 80–86.

Broberg, K.B., 1999. Intersonic crack propagation in orthotropic material. International Journal of Fracture 99 (1–2), 1–11.

Camacho, G.T., Ortiz, M., 1996. Computational modelling of impact damage in brittle materials. International Journal of Solids and Structures 33 (20–22), 2899–2938.

Christensen, R.M., 1979. Mechanics of composite materials. Wiley, New York.

Coker, D., Rosakis, A.J., 1998. Experimental observations of intersonic crack growth in asymmetrically loaded unidirectional composites plates. SM Report, pp. 1–34.

Coker, D., Rosakis, A.J., 2001. Experimental observations of intersonic crack growth in asymmetrically loaded unidirectional composites plates. Philosophical Magazine A 81 (3), 571–595.

Corigliano, A., 1993. Formulation, identification and use of interface models in the numerical analysis of composite delamination. International Journal of Solids and Structures 30, 2779–2811.

Dugdale, D.S., 1960. Yielding of steel sheets containing slits. Journal of the Mechanics and Physics of Solids 8, 100–104.

Freund, L.B., 1979. The mechanics of dynamic shear propagation. Journal of Geophysical Research 84 (B5), 2199–2209.

Freund, L.B., 1989. Dynamic Fracture Mechanics. Cambridge University Press, Cambridge.

Gao, H.J., Huang, H., Gumbsch, P., Rosakis, A.J., 1999. On radiation-free transonic motion of cracks and dislocations. Journal of the Mechanics and Physics of Solids 47 (9), 1941–1961.

Georgiadis, H.G., 1986. On the stress singularity in steady-state transonic shear crack-propagation. International Journal of Fracture 30 (3), 175–180.

Giannakopoulos, A.E., 1989. The return mapping method for the integration of friction constitutive relations. Computers and Structures 32 (1), 157–167.

Huang, Y., Wang, W., Liu, C., Rosakis, A., 1998. Intersonic crack growth in bimaterial interfaces: an investigation of crack face contact. Journal of the Mechanics and Physics of Solids 46 (11), 2233–2259.

Huang, Y., Wang, W., Liu, C., Rosakis, A., 1999. Analysis of intersonic crack growth in unidirectional fiber-reinforeced composites. Journal of the Mechanics and Physics of Solids 47 (9), 1893–1916.

Hughes, T.J.R., 1983. Analysis of transient algorithms with particular reference to stability behavior. In: Belytschko, T., Hughes, T.J.R. (Eds.), Computational Methods for Transient Analysis. North-Holland, Amsterdam, pp. 67–155.

Lambros, J., Rosakis, A.J., 1995a. Development of a dynamic decohesion criterion for subsonic fracture of the interface between two dissimilar materials. Proceedings of the Royal Society of London A 451, 711–736.

Lambros, J., Rosakis, A.J., 1995b. Shear dominated transonic crack growth in bimaterials-part i: experimental observations. Journal of the Mechanics and Physics of Solids 43 (2), 168–188.

Liu, C., Huang, Y., Rosakis, A.J., 1995. Shear dominated transonic interfacial crack growth in a bimaterial-ii. Asymptotic fields and favorable velocity regimes. Journal of the Mechanics and Physics of Solids 43 (2), 198–206.

Liu, C., Rosakis, A.J., Ellis, R.W., Stout, M.G., 1998. A study of the fracture behavior of unidirectional fiber-reinforced composite using coherent gradient sensing (cgs) interferometry. International Journal of Fracture 90 (4), 355–382.

Needleman, A., 1999. An analysis of intersonic crack growth under shear loading. Journal of Applied Mechanics 66, 847–857.

Needleman, A., Rosakis, A.J., 1999. The effect of bond strength and loading rate on the conditions governing the attainment of intersonic crack growth along an interface. Journal of the Mechanics and Physics of Solids 47 (12), 2411–2449.

Ortiz, M., Pandolfi, A., 1999. A class of cohesive elements for the simulation of three-dimensional crack propagation. International Journal for Numerical Methods in Engineering 44, 1267–1282.

Pandolfi, A., Krysl, P., Ortiz, M., 1999. Finite element simulation of ring expansion and fragmentation. International Journal of Fracture 95, 279–297.

Pandolfi, A., Ortiz, M., 1998. Solid modeling aspects of three-dimensional fragmentation. Engineering with Computers 14 (4), 287–308.

Pandolfi, A., Ortiz, M., 2002. An efficient adaptive procedure for three-dimensional fragmentation simulations. Engineering with Computers 18 (2), 148–159.

Piva, A., Hasan, W., 1996. Effect of orthotropy on the intersonic shear crack propagation. Journal of Applied Mechanics 63 (4), 933–938.

Rice, J.R., 1968. Mathematical analysis in the mechanics of fracture. In: Liebowitz, H. (Ed.), Fracture. Academic Press, New York, pp. 191–311.

Rosakis, A.J., Samudrala, O., Coker, D., 1999. Cracks faster than the shear wave speed. Science 284 (5418), 1337–1340.

Rosakis, A.J., Samudrala, O., Coker, D., 2000. Intersonic shear crack growth along weak planes. Materials Research Innovations 3 (4), 236–243.

Rosakis, A.J., Samudrala, O., Singh, R.P., Shukla, A., 1998. Intersonic crack propagation in bimaterial systems. Journal of the Mechanics and Physics of Solids 46 (10), 1789–1813.

Ruiz, G., Ortiz, M., Pandolfi, A., 2000. Three-dimensional finite-element simulation of the dynamic brazilian tests on concrete cylinders. International Journal for Numerical Methods in Engineering 48 (7), 963–994.

Ruiz, G., Pandolfi, A., Ortiz, M., 2001. Three-dimensional cohesive modeling of dynamic mixed-mode fracture. International Journal for Numerical Methods in Engineering 52 (1–2), 97–120.

Singh, R.P., Lambros, J., Shukla, A., Rosakis, A.J., 1997. Investigation of the mechanics of intersonic crack propagation along a bimaterial interface using coherent gradient sensing and photoelasticity. Proceedings of the Royal Society of London A 453, 2649–2667.

Singh, R.P., Shukla, A., 1996. Intersonic crack propagation in bimaterial systems. Journal of Applied Mechanics 63 (4), 919–924.

Tippur, H.V., Krishnaswamy, S., Rosakis, A.J., 1990. Coherent gradient sensor for crack tip deformation measurements: analysis and experimental results. International Journal of Fracture 48, 193–204.

Tippur, H.V., Krishnaswamy, S., Rosakis, A.J., 1991. Optical mapping of crack tip deformations using the method of transmission and reflection coherent gradient sensing: a study of crack tip *k*-dominance. International Journal of Fracture 52, 91–117.

Zehnder, A.T., Guduru, P.R., Rosakis, A.J., Ravichandran, G., 2000. Million frames per second infrared imaging system. Review of Scientific Instruments 71, 3762–3768.